Hypersensitive Tunable Josephson Escape Sensor for Gigahertz Astronomy

Federico Paolucci [1,2,*] Nadia Ligato,[2] Vittorio Buccheri,[1,2] Gaia Germanese [2,3] Pauli Virtanen,[4] and Francesco Giazotto [2,†]

[1] *INFN Sezione di Pisa, Largo Bruno Pontecorvo 3, Pisa 56127, Italy*

[2] *NEST, Istituto Nanoscienze Consiglio Nazionale delle Ricerche and Scuola Normale Superiore, 56127 Pisa, Italy*

[3] *Dipartimento di Fisica dell'Università di Pisa, Largo Pontecorvo 3, 56127 Pisa, Italy*

[4] *Department of Physics and Nanoscience Center, University of Jyvaskyla, P.O. Box 35 (YFL), FI-40014 Jyväskylä, Finland*

Single-photon detectors and bolometers represent the bridge between different topics in science, such as quantum computation, astronomy, particle physics, and biology. Nowadays, superconducting bolometers and calorimeters are the most-sensitive detectors in the terahertz and subterahertz bands. Here, we propose and demonstrate a Josephson escape sensor (JES) that could find natural application in astrophysics. The JES is composed of a fully superconducting one-dimensional Josephson junction, whose resistance-versus-temperature characteristics can be precisely controlled by a bias current. Therefore, differently from traditional superconducting detectors, the JES sensitivity and working temperature can be *in situ* simply and finely tuned depending on the application requirements. A JES bolometer is expected to show an intrinsic thermal-fluctuation-noise noise-equivalent power on the order of 10^{-25} W/Hz$^{1/2}$, while a JES calorimeter could provide a frequency resolution of about 2 GHz, as deduced from the experimental data. In addition, the sensor can operate at the critical temperature (i.e., working as a conventional transition-edge sensor), with a noise-equivalent power of approximately 6×10^{-20} W/Hz$^{1/2}$ and a frequency resolution of approximately 100 GHz.

I. INTRODUCTION

Sensitive photon detection in the gigahertz band constitutes the cornerstone to study different phenomena in astronomy [1], such as radio-burst sources [2], galaxy formation [3], the cosmic microwave background [4], axions [5,6], comets [7], gigahertz-peaked-spectrum radio sources [8], and supermassive black holes [9]. Nowadays, state-of-the-art detectors for astrophysics are mainly based on transition-edge sensors [10–12] and kinetic inductance detectors [13–15]. Overall, most sensible nanobolometers so far are superconducting detectors [16] showing a noise-equivalent power (NEP) as low as approximately 2×10^{-20} W/Hz$^{1/2}$ [17]. Yet, fast thermometry at the nanoscale was demonstrated as well with Josephson junctions (JJs) through switching-current measurements [18,19]. In general, detection performance is set by the fabrication process and is limited by the materials used.

In this work, we conceive and demonstrate a tunable Josephson escape sensor (JES) based on the precise current control of the temperature dependence of a fully superconducting one-dimensional nanowire Josephson junction. The JES might be at the core of future hypersensitive *in situ*–tunable bolometers or single-photon detectors working in the gigahertz regime. Operated as a bolometer, the JES has a NEP due to thermal-fluctuation noise (TFN), NEP$_{\text{TFN}}$, of approximately 1×10^{-25} W/Hz$^{1/2}$, which as a calorimeter bounds the frequency resolution above approximately 2 GHz, and resolving power reaching approximately 40 at 50 GHz, as deduced from the experimental data.

Beyond the obvious applications in advanced ground-based [20] and space [21] telescopes for gigahertz astronomy, the JES might represent a breakthrough in several fields of quantum technologies ranging from subterahertz communications [22] and quantum computing [23] to cryptography [24] and quantum key distribution [25].

II. GIGAHERTZ ASTROPHYSICS AND JES OPERATION PRINCIPLE

Many features of the universe are hidden in infrared and microwave faint signals [1]. In particular, the study of cosmic-microwave-background polarization [4,26] and galaxy expansion [3] benefits from ultrasensitive gigahertz bolometers, while the existence of axionlike particles

---

*federico.paolucci@nano.cnr.it

†francesco.giazotto@sns.it
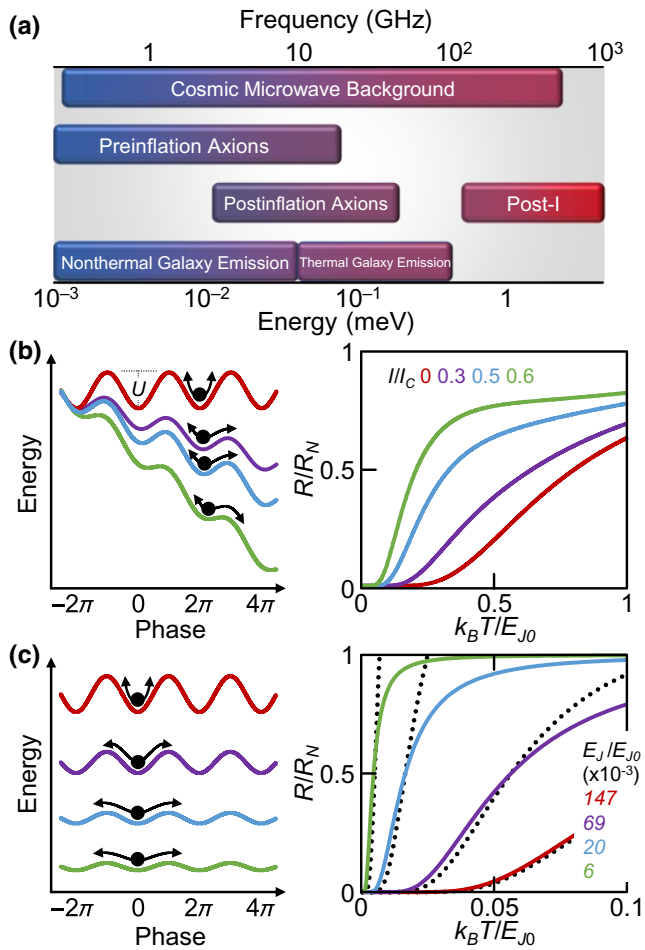
(a)

(b)

(c)

FIG. 1. Gigahertz astronomy and JES operation principle. (a) Frequency and energy ranges relevant for different astronomical investigations, such as cosmic microwave background [4], preinflation and postinflation axions (Post-I) [6], and nonthermal and thermal galaxy emission [3]. (b) The left panel shows the schematics of the washboard model versus the phase difference across a JJ for different values of bias current (I rises from red to green, with the same color code in the right panel). U represents the energy barrier for the escape of the phase particle (black dots). The right panel shows the resistance- (R) versus-temperature (T) characteristics of a JJ for different values of I. Both the transition temperature and its width decrease with increasing I. (c) The left panel shows the schematics of the washboard model versus the phase difference across a JJ for different values of the Josephson energy (E_J decreases from red to green, with the same color code in the right panel). The right panel shows the R-versus-T characteristics of a JJ for different values of E_J at $I = 0$. Dotted black curves are calculated for $E_J = E_{J0}$ by our varying I to have the same transition temperature.

[5,6] might be proven through the revelation of microwave single photons [see Fig. 1(a)].

To increase photon-detection sensitivity, novel superconducting sensors have been developed by miniaturizing the active region [27,28] and drastically lowering their operation temperature via the Josephson coupling in complex nanostructures [17,29–35]. Their properties are thus defined during the fabrication process and cannot be tuned during the operation. In analogy to the widespread transition-edge sensor (TES), the JES exploits the change of resistance of a superconductor when transitioning to the dissipative state: either the absorption of radiation or the change of temperature [18,19] triggers the passage from the superconducting regime to the normal regime, yielding a sizable signal from the sensor. In contrast to TESs, the JES benefits from the possibility to finely tune *in situ* its working temperature and sensitivity.

The JES operation principle is based on a fully superconducting one-dimensional (1D) JJ (i.e., two superconducting leads coupled by a superconducting nanowire with lateral dimensions smaller than its coherence length, ξ). The transition to the dissipative state can be understood as being due to 2π phase slips, qualitatively similar to the tilted-washboard-potential (WP) model of JJs, where a phase particle moves in the WP under the action of friction forces [36,37]. The effective WP profile strongly depends on both the bias current (I) through the junction and Josephson energy (E_J) [38] [see the left panels in Figs. 1(b) and 1(c)]. In particular, for a 1D nanowire JJ, the escape barrier can be written as [38]

$$U(I, E_J) \simeq 2E_J (1 - I/I_C)^{5/4}, \qquad (1)$$

where $E_J = \Phi_0 I_C/2\pi$, $\Phi_0 \simeq 2.067 \times 10^{-15}$ Wb is the flux quantum, and I_C is the JJ critical current. Equation (1) shows that the phase-particle escape from a potential minimum (and, therefore, the corresponding transition of the junction to the dissipative state) can be finely controlled either by increasing I or by reducing E_J.

Because of the use of a 1D JJ, the JES benefits from a twofold advantage. On the one hand, transverse dimensions smaller than ξ ensure a constant superconducting wave function along the wire cross section, leading to uniform superconducting properties. On the other hand, a nanowire width (w) much smaller than the London penetration depth (λ_L) guarantees a homogeneous supercurrent density in the JJ when the JES is current biased and an uniform penetration of the film by an external magnetic field.

For comparison, in a sufficiently shunted overdamped limit, we can evaluate the resistance- (R) versus-temperature (T) characteristics of a JJ for different values of I and E_J by calculating the current derivative of the voltage drop [39]:

$$V(I, E_J, T) = R_N \left(I - I_{C,0} \, \mathrm{Im} \, \frac{\mathcal{I}_{1-iz}\left(\frac{E_J}{k_B T}\right)}{\mathcal{I}_{-iz}\left(\frac{E_J}{k_B T}\right)} \right), \qquad (2)$$

where $I_{C,0}$ is the JJ zero-temperature critical current, $\mathcal{I}_\mu(x)$ is the modified Bessel function with imaginary argument

μ, and $z = (E_J/k_B T)(I/I_C)$. The details of the theoretical model are given in Supplemental Material [40].

Specifically, an increase of I leads to a sizable lowering of the resistive transition temperature accompanied by narrowing of its width, as shown in the right panel in Fig. 1(b) for $E_J = E_{J0}$ (where E_{J0} is the zero-temperature Josephson energy). Similarly, the transition temperature can be reduced by decreasing E_J, but its width becomes wider than in the presence of a sizable bias current flowing through the nanowire [see the right panel in Fig. 1(c)]. The dotted black curves are calculated for $E_J = E_{J0}$ by our varying I in order to have the same transition temperature (T_C) given by the reduction of the Josephson energy. The temperature response of R originating from the bias current yields transitions that are sharper than those obtained by simply reducing E_J.

E_J can be reduced, for instance, by applying an external magnetic field (B). However, the use of external magnetic field can be detrimental for several applications, since it typically broadens the superconducting transition [41]. As we show, tuning the nanowire JJ through current injection will prove to be an excellent strategy to achieve near-to-ideal nanosensors with excellent performance.

III. JES STRUCTURE AND BASIC CHARACTERIZATION

The realization of a typical JES is shown in the pseudo-color scanning electron micrograph displayed in Fig. 2(a). The JESs are fabricated by electron-beam lithography and two-angle shadow-mask electron-beam evaporation of metals onto an oxidized silicon wafer through a suspended resist mask. The 1D-sensor active region consists of a bilayer of Al ($t_{Al} = 10.5$ nm) and Cu ($t_{Cu} = 15$ nm) evaporated at an angle of $0°$. The total volume of the sensor active region is $\mathcal{V}_w = \mathcal{V}_{Al} + \mathcal{V}_{Cu} \simeq 3.83 \times 10^{-21}$ m^{-3}, with $\mathcal{V}_{Al} \simeq 1.58 \times 10^{-21}$ m^{-3} and $\mathcal{V}_{Cu} \simeq 2.25 \times 10^{-21}$ m^{-3}. The lateral 40-nm-thick Al banks are then evaporated at an angle of $40°$.

All measurements are performed in a filtered He^3-He^4 dry dilution refrigerator at different bath temperatures in the range from 20 to 160 mK. The resistance-versus-temperature characteristics of the JES and of the Al banks are obtained by conventional the four-wire low-frequency lock-in technique at 13.33 Hz. To this end, ac excitation currents with typical root-mean-square amplitudes $I \simeq$ 15–380 nA are imposed through the device. The current is generated by our applying an ac voltage bias (V_{ac}) to a load resistor of impedance (R_L) much larger than the sample resistance ($R_L = 100\,\text{k}\Omega \gg R$). The critical temperature of the Al banks is measured with the same setup. The I-versus-V characteristics of the nanowires are obtained by our applying a low-noise dc bias current, while the voltage drop is measured via a room-temperature battery-powered differential preamplifier.
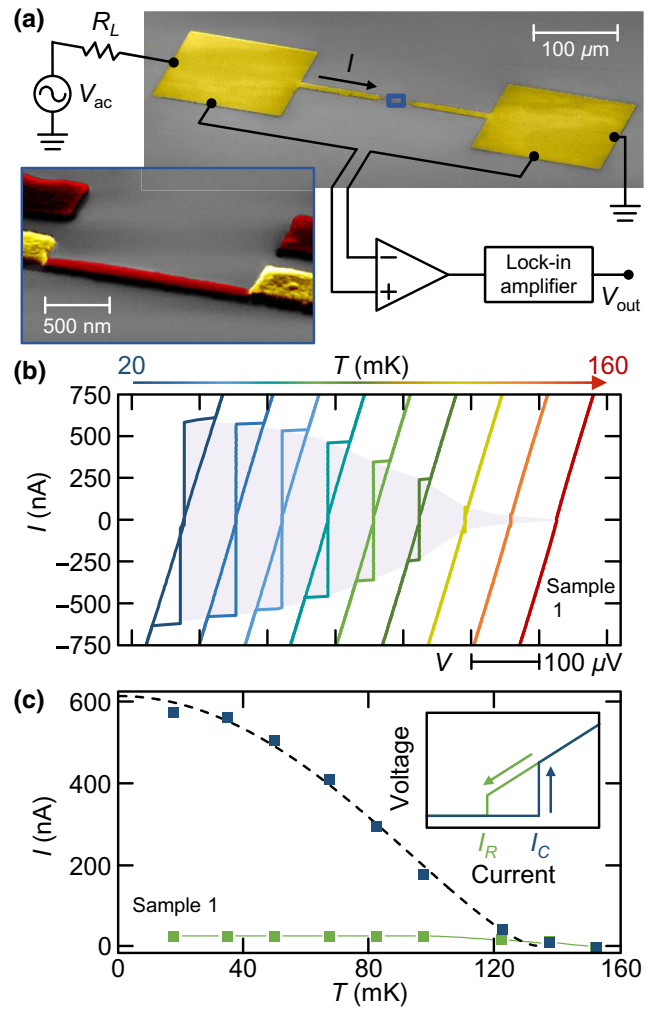

FIG. 2. Realization of the JES. (a) False-color scanning electron micrograph of a typical JES. The nanosensor is ac-biased (amplitude I) and the voltage drop across the wire (V_{out}) is measured via a voltage preamplifier connected to a lock-in amplifier. R_L is a high-impedance load resistor. The inset shows an enlargement of the core of the JES showing the Al/Cu nanowire (red) in contact with thick Al leads (yellow). (b) Back-and-forth dc current-vs-voltage (I-V) characteristics of a typical JES measured at different temperatures T ranging from 20 to 160 mK in steps of approximately 20 mK. The curves are horizontally shifted for clarity. (c) Temperature evolution of the critical current (I_C; blue) and the retrapping current (I_R; green). The dashed black line is the critical-current prediction of the Bardeen model [43] (see the Appendix for details). The green line is a guide for the eye for the retrapping current. The inset shows the nanowire switches from the superconducting state to the normal state at I_C, while the transition from the resistive regime to the dissipationless regime occurs at I_R. The hysteretic behavior stems from Joule heating during transitioning from the normal state to the superconducting state [42]. I_R is almost temperature independent, and it is approximately 26.6 nA.

Josephson transport in the nanosensor is highlighted by the I-versus-V characteristics shown in Fig. 2(b) for bath temperatures (T) ranging from 20 to 160 mK. The

wire normal-state resistance $R_N \simeq 77\,\Omega$, and the typical heating-induced hysteretic behavior of the $I–V$ curves is observed [42]. On the one hand, the critical current is maximum ($I_C \simeq 575$ nA) at $T \simeq 20$ mK [see Fig. 2(c)] and monotonically decreases with temperature following the prediction of Bardeen [43] (see the Appendix for details). On the other hand, the retrapping current ($I_R \simeq 26.6$ nA) is constant in the whole temperature range.

As stated, the JES working principle is based on a 1D nanowire JJ. Indeed, the coherence length ($\xi \simeq 220$ nm) and the London penetration depth ($\lambda_L \simeq 970$ nm) of the nanowire are much greater than the wire width ($w = 100$ nm) and total film thickness ($t_w = 25.5$ nm), thereby providing the frame of a 1D junction (see the Appendix). Yet, the nanowire length (approximately 6.8ξ) reduces the influence of the superconducting proximity effect arising from the clean contact with the lateral Al leads [37]. We also note that the maximum magnetic field created by the critical-current flow, $B_{\max} \simeq 5\,\mu$T, is negligibly small compared with the out-of-plane critical magnetic field of the wire ($B_C \simeq 21$ mT), thus implying a vanishing effect on the JES.

IV. CURRENT MODULATION OF THE R-VERSUS-T CHARACTERISTICS

We investigate the behavior of the JES by recording the resistance-versus-temperature characteristics for several amplitudes I of low-frequency ac bias current [see Fig. 3(a)]. The $R(T)$ characteristics monotonically shift toward low temperatures with increasing I, almost preserving the same shape up to the largest current amplitude. In particular, I is varied between approximately 3% and approximately 64% of I_C. Although the transition curves shift toward low T with increasing I, the nanowire electronic temperature T_w in the middle of the transition under current injection is not expected to coincide anymore with the bath temperature T_b. Indeed, when the sensor is transitioning to the normal state, electrons in the nanowire are Joule overheated with respect to T_b by the bias current (with final $T_w \lesssim T_C$), thus preventing the operation of the nanosensor as a conventional TES biased at those low bath temperatures, without additional shunting. By contrast, when the sensor is operated in the dissipationless regime (i.e., as an escape sensor), T_w coincides with T_b.
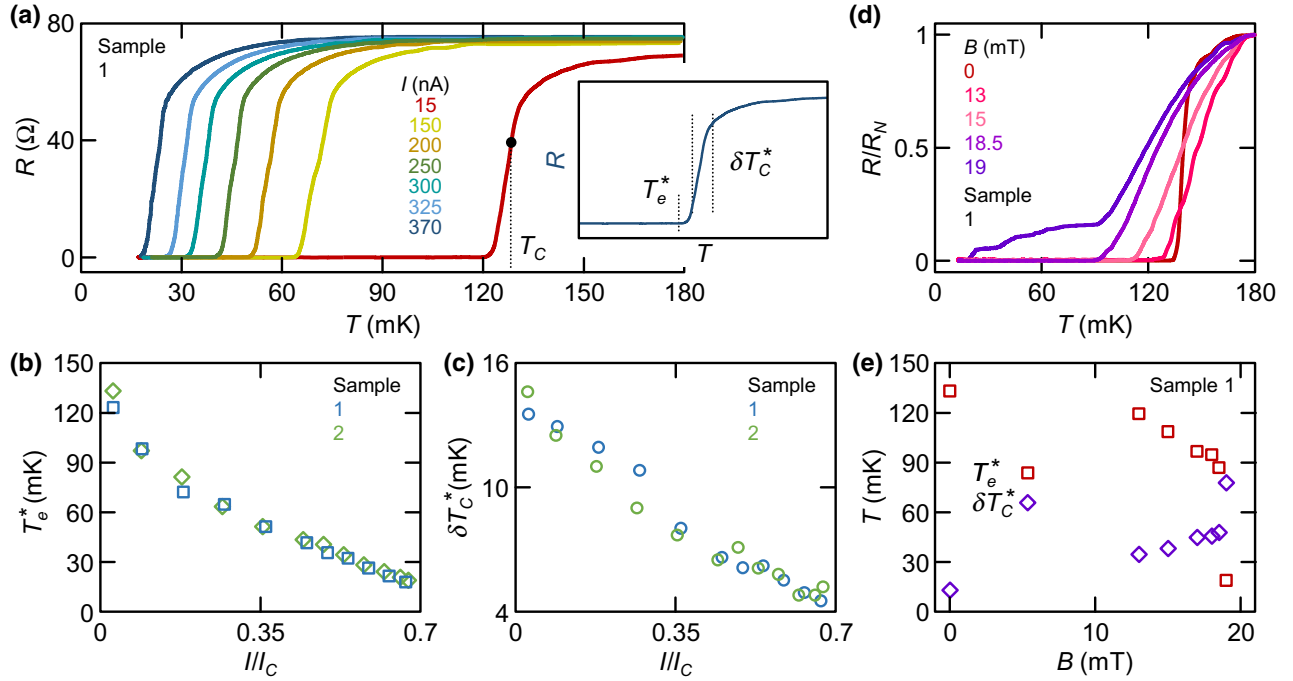

FIG. 3.   Tuning the properties of the JES. (a) Selected resistance- (R) versus-temperature (T) characteristics for different values of ac-bias-current amplitude I. The inset shows a sketch of the temperature dependence of the JES resistance. The current-dependent escape temperature T_e^* and the phase-transition width δT_C^* are indicated. T_e^* monotonically decreases with increasing I, while the transition becomes sharper with increasing bias current. $T_C \simeq 130$ mK is the critical temperature of sample 1. (b) Full behavior of T_e^* versus I for two different JESs. For large I, T_e^* can be as small as approximately 20 mK. (c), Width of the phase transition δT_C^* versus I for two different JESs. δT_C^* is reduced by a factor of 4 at the largest bias currents. Note the fine tunability of T_e^* provided by the injection current. (d) R-versus-T characteristics for different values of the perpendicular-to-plane magnetic field (B). The sizable widening of the phase transition likely stems from depairing in the nanowire induced by the magnetic field [41]. (e) T_e^* and δT_C^* versus B. T_e^* shifts toward lower values with increasing B, but the transition becomes much broader at higher fields. Yet, T_e^* is hardly tunable at large values of B.

From the R-versus-T curves we can specify a current-dependent temperature related to the resistive transition; that is, the escape temperature, $T_e^*(I)$. The latter is the maximum value of T providing zero nanowire resistance [see the inset in Fig. 3(a) and the Appendix]. The $T_e^*(I)$ characteristics for two JES samples are shown in Fig. 3(b). In particular, T_e^* is monotonically reduced by increase of I, with a minimum value of approximately 20 mK for $I = 370$ nA, corresponding to approximately 15% of the nanowire intrinsic critical temperature, $T_C \simeq 130$ mK. Moreover, the transition width (δT_C^*) narrows with increasing I [see Fig. 3(c)]. In particular, δT_C^* is reduced by a factor of 4 at the largest current amplitude, mirroring the expected changes in the switching as shown in Fig. 1(b).

In addition, to prove the complementary tuning of the WP through the reduction of I_C [see Eq. (1)], we apply a perpendicular-to-plane magnetic field. The resulting shape of the corresponding transition degrades dramatically in the presence of an external magnetic field [see Fig. 3(d)]. In particular, the R-versus-T characteristics appear to be scarcely tunable, while the onset of the transition is almost unaffected. The extreme broadening of the transition from the superconducting state to the dissipative state can be explained in terms of flux penetration in the nanowire and in the aluminum banks, since our nanowires are thinner than the London penetration depth for a magnetic field (see the Appendix for details). T_e^* shows a stark variation at values of $B \to B_C$, together with the strong enlargement of the transition width, as displayed in Fig. 3(e). The above results in a finite magnetic field validate therefore the bias current as an ideal tool to control the JES properties.

V. PERFORMANCE OF JES-BASED BOLOMETERS AND CALORIMETERS

Insight into the behavior of the JES can be gained by considering the predominant heat-exchange mechanisms occurring in the nanodevice, as schematically depicted in the thermal model in Fig. 4(a). The absorption of external incident radiation (P_{in}) leads to the increase of the nanowire electronic temperature T_w. Yet, the two lateral superconducting Al leads (residing at bath temperature
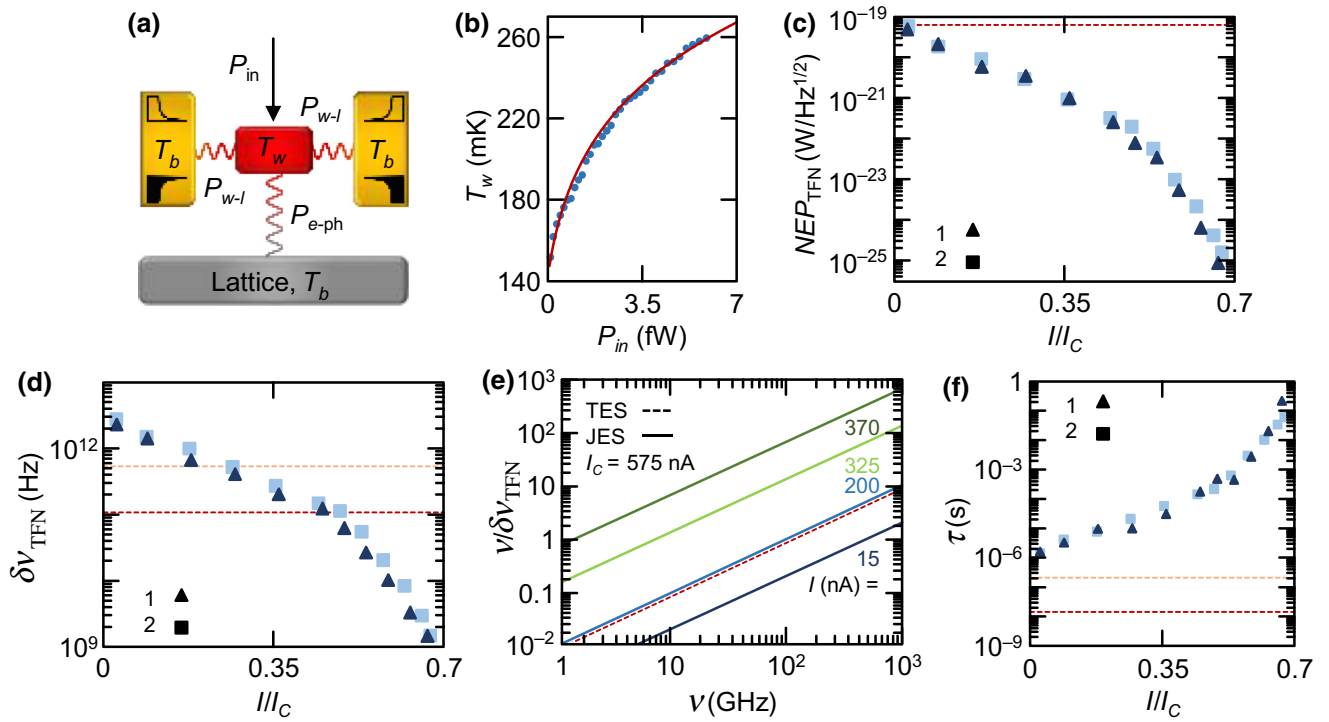

FIG. 4. Performance of the JES. (a) Thermal model highlighting the predominant heat-exchange mechanisms occurring in the nanosensor. P_{in} is the power coming from the incident radiation, $P_{e\text{-ph}}$ is the heat exchanged between electrons in the nanowire residing at temperature T_w (red box) and lattice phonons residing at bath temperature T_b (gray box), and $P_{w\text{-}l}$ is the electron heat current flowing from the nanowire to the superconducting leads residing at T_b (yellow boxes). (b) Electronic temperature in the nanowire T_w (blue dots) versus P_{in} recorded at $T_b = 147.5$ mK. The red line represents the theoretical behavior (see Supplemental Material for details [40]). (c) Deduced NEP_{TFN} versus I for sample 1 (triangles) and sample 2 (squares). (d) Frequency resolution $\delta\nu_{TFN}$ versus I for sample 1 (triangles) and sample 2 (squares). (e) Resolving power $\nu/\delta\nu_{TFN}$ versus frequency ν calculated for sample 1. $\nu/\delta\nu_{TFN}$ increases with increasing bias current (from blue to green). (f) Time constant τ versus I for sample 1 (triangles) and sample 2 (squares). The dashed lines in (c)–(f) indicate the expected figures of merit when the sensor is operated at T_C in TES mode for sample 1 (red) and sample 2 (yellow).

T_b) serve as Andreev mirrors [44], thereby suppressing heat out-diffusion (P_{w-l}) from the nanowire. As a consequence, the main thermal relaxation channel in the system stems from heat exchange with lattice phonons ($P_{e\text{-ph}}$) residing at T_b. For a normal metallic thin film, $P_{e\text{-ph},n} = \Sigma_w \mathcal{V}_w \left(T_w^5 - T_b^5 \right)$ [10,45], where $\mathcal{V}_w$ is the nanowire volume and Σ_w is the electron-phonon coupling constant of the bilayer. Σ_w is determined through energy-relaxation experiments [45] by our injecting a known power, and by our measuring the resulting steady-state electron temperature established in an *ad hoc*–fabricated identical wire kept above its critical temperature. Figure 4(b) shows the T_w-versus-P_{in} characteristics (blue dots) recorded at $T_b = 147.5$ mK along with a fit to the data, which allows us to extract the electron-phonon coupling constant in the Al/Cu nanowire, $\Sigma_w \simeq 1.15 \times 10^9$ W/m^3 K^5 (see Supplemental Material [40]).

Yet, since the JES is operated in the superconducting state at $T_e^*(I)$, the latter can be substantially smaller than T_C depending on the current amplitude. At sufficiently low temperature, the electron-phonon heat exchange in a superconductor is exponentially suppressed with respect to the normal state owing to the presence of the energy gap; that is, $P_{e\text{-ph},s} \propto P_{e\text{-ph},n} \exp \left[-\Delta_w / (k_B T_e^*) \right]$ [46], where $\Delta_w \simeq 23$ μeV is the pairing potential in the nanowire (see Supplemental Material for details [40]). As we argue later, the operation deep in the superconducting state dramatically increases the JES radiation detection sensitivity.

In general, the performance of a bolometer can be quantified by the NEP; that is, the input-power resolution per unit bandwidth. For the JES, the NEP is bounded by thermal fluctuations between the electron-and-phonon system in the nanowire [45]. Other limitations to the resolution can arise from the switching measurement, which we assume is optimized to be subdominant. NEP$_{\text{TFN}}$ can be extracted by our substituting the measured parameters of the JES, such as I_C-versus-T and $R(T)$ characteristics, Δ_w, and Σ_w, in the widely used equations for superconducting radiation sensors [45] (see also Supplemental Material [40]). NEP$_{\text{TFN}}$ monotonically decreases with increasing current amplitude, and is *in situ* finely controlled by tuning I [see Fig. 4(c)]. In particular, the JES has noise values that are several orders of magnitude smaller than previously reported. Specifically, the best extracted NEP$_{\text{TFN}}$ is low as approximately 1×10^{-25} W/$\sqrt{\text{Hz}}$ for $I = 370$ nA at approximately 18 mK. By contrast, in the normal state (i.e., when the JES is operated as a conventional TES), the sensor is expected to provide a much higher NEP$_{\text{TFN}}$ of approximately 6×10^{-20} W/$\sqrt{\text{Hz}}$ because the electron-phonon thermalization in the active region is stronger.

In pulsed detection mode, a relevant figure of merit of a radiation sensor is the frequency resolution ($\delta\nu$); that is, the minimum detectable energy for an incident single photon (see Supplemental Material for details [40]). We assume the JES measurement is performed accurately and

sufficiently fast [18,19] compared with the thermal relaxation time τ, and estimate the limitation from the TFN. Figure 4(d) emphasizes the strong dependence of $\delta\nu_{\text{TFN}}$ on I, which displays variations over 3 orders of magnitude. For $\delta\nu_{\text{TFN}}$, this limit can be as low as approximately 2 GHz at 370 nA, and would enable single-photon sensing at unprecedented low energies. When the nanosensor is operated as as TES, $\delta\nu$ is roughly 2 orders of magnitude larger, and is approximately 100 GHz. The limitation to single-photon sensing capability from TFN in our JES is highlighted by the resolving power ($\nu/\delta\nu_{\text{TFN}}$), which is shown versus the incident-radiation frequency in Fig. 4(e). $\nu/\delta\nu_{\text{TFN}}$ can reach approximately 40 at 50 GHz and approximately 800 at 1 THz, both for 370 nA, whereas it can be approximately 10 at 1 THz when the sensor is operated as a TES. Since the power associated with 1-THz photons is lower than 1×10^{-18} W and the power dissipated through the phonons at $T = 260$ mK is about 6 fW [see Fig. 4(b)], the electronic temperature in the wire is always lower than $0.3T_{C,\text{Al}}$. Therefore, we can exclude thermal diffusion through the aluminum banks [44], thus considering the active region to be fully thermally isolated from the electrodes.

We finally comment on the JES time constant (τ), which is one of the fundamental figures of merit for a radiation sensor. It is basically given by the ratio between the electron heat capacitance and the electron-phonon heat conductance in the nanowire [45], since heat conduction through the lateral electrodes is negligible in a JES. In pulsed detection mode, τ determines the minimum speed of the readout electronics (which has to be faster than the time constant) and the minimum time separation for the independent detection of two photons. Figure 4(f) shows the expected JES time constant versus bias current I, as deduced from the experimental data (see Supplemental Material for details [40]). In particular, τ increases monotonically with increasing I, and varies between approximately 1 μs at low current amplitude and approximately 100 ms at 370 nA. In general, when used at T_C as a TES, the nanosensor can provide a much-faster response than the JES in the whole bias current range ($\tau \sim 10$–100 ns) because of the higher operation temperature and electron-phonon thermal relaxation.

VI. CONCLUSIONS

We conceive and demonstrate an innovative hypersensitive superconducting radiation-sensing element with the capability of *in-situ* fine tuning its performances by a current bias. Our nanosensor has the potential to drive radiation detection in the gigahertz regime toward unexplored levels of sensitivity by lowering the thermal-fluctuation limitation to NEP down to approximately 1×10^{-25} W/$\sqrt{\text{Hz}}$, with a corresponding limit in frequency resolution of approximately 2 GHz. The JES is expected to

have a significant impact in radio astronomy [1–4,7,9,20, 21], space spectroscopy [8], and dark-matter search [5,6] since its working mechanism could allow, in principle, the immediate replacement of TESs in already-existing experiments and telescopes. Furthermore, the JES could have countless applications in several fields of quantum technology, where extrasensitive photon detection is a fundamental task, such as subterahertz communication [22], quantum computation [23], and quantum cryptography [24,25].

ACKNOWLEDGMENTS

APPENDIX: DEVICE PARAMETERS

The temperature dependence of the critical current of the nanowire can be fitted through the phenomenological equation [43] $I_C(T) = I_{C,0} \left[1 - (T/T_C)^2\right]^{3/2}$, where $I_{C,0}$ is the zero-temperature critical current. The fit provides $I_{C,0} \simeq 615$ nA and critical temperature $T_{C,\text{fit}} \simeq 133$ mK, which is in good agreement with the experimental value obtained from the resistance-versus-temperature characteristics.

The Al/Cu bilayer can be considered as a uniform superconductor since it lies within the Cooper limit [47, 48]. We assume a transparent Al/Cu interface. Moreover, the aluminum layer respects $t_{\text{Al}} = 10.5$ nm $\ll \xi_{\text{Al}} = \sqrt{\hbar D_{\text{Al}}/\Delta_{\text{Al}}} \simeq 80$ nm (with $\hbar$ the reduced Planck constant, $D_{\text{Al}} = 2.25 \times 10^{-3}$ m^2/s the diffusion constant of Al, and $\Delta_{\text{Al}} \simeq 200\,\mu$eV its superconducting energy gap), while the copper film obeys $t_{\text{Cu}} = 15$ nm $\ll \xi_{\text{Cu}} = \sqrt{\hbar D_{\text{Cu}}/2\pi k_B T} \simeq 255$ nm (with $D_{\text{Cu}} = 8 \times 10^{-3}$ m^2/s the copper diffusion constant and the temperature is chosen for the worst-case scenario, $T = 150$ mK).

From the nanowire normal-state resistance ($R_N \simeq 77\,\Omega$) we determine the superconducting coherence length in the active region $\xi = \sqrt{l\hbar/[(t_{\text{Al}}N_{\text{Al}} + t_{\text{Cu}}N_{\text{Cu}})R_N e^2 \Delta_w]} \simeq 220$ nm, where e is the electron charge, while $N_{\text{Al}} = 2.15 \times 10^{47}$ J^{-1} m^{-3} and $N_{\text{Cu}} = 1.56 \times 10^{47}$ J^{-1} m^{-3} are the density of states at the Fermi level of aluminum and copper, respectively. As a consequence, the nanowire obeys $t_w = t_{\text{Al}} + t_{\text{Cu}} = 25.5$ nm $\ll \xi$, thus ensuring a constant

pairing potential along the out-of-plane axis. The superconducting energy gap of the bilayer, $\Delta_w = 23\,\mu$eV, is determined by tunnel spectroscopy performed on *ad hoc*–fabricated nominally identical wires equipped with Al tunnel probes. For further details, see Supplemental Material [40]. The London penetration depth is determined as $\lambda_L = \sqrt{\hbar(t_{\text{Al}} + t_{\text{Cu}})wR_N/(\pi\mu_0 l\Delta_w)} \simeq 970$ nm, where μ_0 is the vacuum magnetic permeability. The maximum magnetic field generated by the bias current at the wire surface reads $B_{I,\text{max}} = \mu_0 I_{C,0}/2\pi t_w \simeq 5\,\mu$T, where $I_{C,0}$ is the zero-temperature critical current and $t_w = t_{\text{Al}} + t_{\text{Cu}}$ is the total thickness of the JES active region. Finally, the critical temperature of the Al banks is approximately 1.3 K.

The energy gap induced by the lateral Al banks in a nonsuperconducting Al/Cu bilayer is given by $E_g \simeq 3\hbar D_w/L^2 \simeq 5\,\mu$eV, where $D_w = (D_{\text{Al}}t_{\text{Al}} + D_{\text{Cu}}t_{\text{Cu}})/t_w \simeq 5.6 \times 10^{-3}$ m^2/s is the wire diffusion coefficient and $L = 1.5\,\mu$m is its length. This value is less than one quarter of the measured gap. Therefore, the intrinsic superconductivity of the bilayer dominates.

The current-dependent escape temperature $[T_e^*(I)]$ is defined as the maximum temperature providing $R(I) = 0$ (i.e., when the JES is in the dissipationless state).

[1] M. Rowan-Robinson, Probing the cold universe, Science **325**, 546 (2009).

[2] B. Marcote, K. Nimmo, J. W. T. Hessels, S. P. Tendulkar, C. G. Bassa, Z. Paragi, A. Keimpema, M. Bhardwaj, R. Karuppusamy, V. M. Kaspi, and et al., A repeating fast radio burst source localized to a nearby spiral galaxy, Nature **577**, 190-194 (2020).

[3] F. S. Tabatabaei, E. Schinnerer, M. Krause, G. Dumas, S. Meidt, A. Damas-Segovia, R. Beck, E. J. Murphy, D. D. Mulcahy, B. Groves, and et. al., The radio spectral energy distribution and star-formation rate calibration in galaxies, ApJ **836**, 185 (2017).

[4] G. Sironi, The frequency spectrum of the cosmic microwave background, New Astron. Rev. **43**, 243 (1999).

[5] L. M. Capparelli, G. Cavoto, J. Ferretti, F. Giazotto, A. D. Polosa, and P. Spagnolo, Axion-like particle searches with sub-THz photons, Phys. Dark Univ. **12**, 37 (2016).

[6] I. G. Irastorza and J. Redondo, New experimental approaches in the search for axion-like particles, Prog. Part. Nucl. Phys. **102**, 89 (2018).

[7] A. Falchi, L. Gagliardi, F. Palagi, G. Tofani, and G. Comoretto, *10.7 GHz Continuum Observations of Comet P/Halley* (Springer, Heidelberg, 1988).

[8] C. P. O'Dea, The compact steep-spectrum and gigahertz peaked-spectrum radio sources, PASP **110**, 493 (1998).

[9] S. Issaoun, M. D. Johnson, L. Blackburn, C. D. Brinkerink, M. Mocibrodzka, A. Chael, C. Goddi, I. Mart-Vidal, J. Wagner, S. S. Doeleman, and et. al., The size shape, and scattering of sagittarius A* at 86 GHz: First VLBI with ALMA, ApJ **871**, 30 (2019).

[10] K. D. Irwin, An application of electrothermal feedback for high resolution cryogenic particle detection, Appl. Phys. Lett. **66**, 1998 (1995).

[11] K. D. Irwin, Seeing with superconductors, Sci. Am. **295**, 86 (2006).

[12] P. Khosropanah, B. Dirks, M. Parra-Borderas, M. Ridder, R. Hijmering, J. van der Kuur, L. Gottardi, M. Bruijn, M. Popescu, J. R. Gao, and H. Hoevers, in *Proc. SPIE 7741, Millimeter, Submillimeter, and Far-Infrared Detectors and Instrumentation for Astronomy V* Vol. 77410L (SPIE, San Diego, 2010).

[13] P. K. Day, H. G. LeDuc, B. A. Mazin, A. Vayonakis, and J. Zmuldzinas, A broadband superconducting detector suitable for use in large arrays, Nature **425**, 817 (2003).

[14] P. J. Visser, J. J. A. Baselmans, J. Bueno, N. Llombart, and T. M. Klapwijk, Fluctuations in the electron system of a superconductor exposed to a photon flux, Nat. Comm. **5**, 3130 (2014).

[15] A. Monfardini, J. Baselmans, A. Benoit, A. Bideaud, O. Bourrion, A. Catalano, M. Calvo, A. D'Addabbo, S. Doyle, J. Goupy, H. Le Sueur, and J. Macias-Perez, in *Proc. SPIE 9914, Millimeter, Submillimeter, and Far-Infrared Detectors and Instrumentation for Astronomy VIII* Vol. 99140N (SPIE, Edinburgh, 2016).

[16] K. Morgan, Hot science with cool sensors, Phys. Today **71**, 28 (2018).

[17] R. Kokkoniemi, J. Govenius, V. Vesterinen, R. E. Lake, A. M. Gunyhó, K. Y. Tan, S. Simbierowicz, L. Grönberg, J. Lehtinen, M. Prunnila, J. Hassel, A. Lamminen, O.-P. Saira, and M. Möttönen, Nanobolometer with ultralow noise equivalent power, Commun. Phys. **2**, 124 (2019).

[18] M. Zgirski, M. Foltyn, A. Savin, K. Norowski, M. Meschke, and J. P. Pekola, Nanosecond Thermometry with Josephson Junctions, Phys. Rev. Appl. **10**, 044068 (2018).

[19] L. B. Wang, O.-P. Saira, and J. P. Pekola, Fast thermometry with a proximity Josephson junction, Appl. Phys. Lett. **112**, 013105 (2018).

[20] P. Ade *et al.*, The simons observatory: Science goals and forecasts, J. Cosmol. Astropart. Phys. **2019**, 056 (2019).

[21] J. S. Adams *et al.*, First operation of TES microcalorimeters in space with the micro-X sounding rocket, J. Low Temp. Phys. **199**, 1062 (2020).

[22] J. Federici and L. Moeller, Review of terahertz and subterahertz wireless communications, J. Appl. Phys. **107**, 111101 (2010).

[23] J. L. O'brien, Optical quantum computing, Science **318**, 1567 (2007).

[24] N. Gisin, G. Ribordy, W. Tittel, and H. Zbiden, Quantum cryptography, Rev. Mod. Phys. **74**, 145 (2002).

[25] W. Tittel, Quantum key distribution breaking limits, Nat. Photonics **13**, 310 (2019).

[26] U. Seljak and M. Zaldarriaga, Signature of Gravity Waves in the Polarization of the Microwave Background, Phys. Rev. Lett. **78**, 2054 (1997).

[27] B. S. Karasik, D. Olaya, J. Wei, S. Pereverzev, M. E. Gershenson, J. H. Kawamura, W. R. McGrath, and A. V. Sergeev, Record-low NEP in hot-electron titanium nanobolometers, IEEE Trans. Appl. Supercond. **17**, 293 (2007).

[28] J. Wei, D. Olaya, B. S. Karasik, S. V. Pereverzev, A. V. Sergeev, and M. E. Gershenson, Ultrasensitive hot-electron nanobolometers for terahertz astrophysics, Nat. Nanotech. **3**, 496 (2008).

[29] Y.-F. Chen, D. Hover, S. Sendelbach, L. Maurer, S. T. Merkel, E. J. Pritchett, F. K. Wilhelm, and R. McDermott, Microwave Photon Counter Based on Josephson Junctions, Phys. Rev. Lett. **107**, 217401 (2011).

[30] C. M. Natarajan, M. G. Tanner, R. H. Hadfield, Superconducting nanowire single-photon detectors: Physics and applications, Supercond. Sci. Technol. **25**, 063001 (2012).

[31] J. Govenius, R. E. Lake, K. Y. Tan, and M. Möttönen, Detection of Zeptojoule Microwave Pulses Using Electrothermal Feedback in Proximity-Induced Josephson Junctions, Phys. Rev. Lett. **117**, 030802 (2016).

[32] L. S. Kuzmin, A. L. Pankratov, A. V. Gordeeva, V. O. Zbrozhnek, V. A. Shamporov, L. S. Revin, A. V. Blagodaktin, S. Masi, and P. de Bernardis, Photon-noise-limited cold-electron bolometer based on strong electron self-cooling for high-performance cosmology missions, Commun. Phys. **2**, 104 (2019).

[33] B. Karimi, F. Brange, P. Samuelsson, and J. P. Pekola, Reaching the ultimate energy resolution of a quantum detector, Nat. Comm. **11**, 367 (2020).

[34] P. Virtanen, A. Ronzani, and F. Giazotto, Josephson Photodetectors via Temperature-To-Phase Conversion, Phys. Rev. Appl. **9**, 054027 (2018).

[35] F. Giazotto, T. T. Heikkilä, G. P. Pepe, P. Helistö, A. Luukanen, and J. P Pekola, Ultrasensitive proximity Josephson sensor with kinetic inductance readout, Appl. Phys. Lett. **92**, 162507 (2008).

[36] A. Barone and G. Paternò, *Physics and Applications of the Josephson Effect* (Wiley-VCH, New York, 1982).

[37] M. Tinkham, *Introduction to Superconductivity* (McGraw-Hill, New York, 1996).

[38] A. Bezryadin, *Superconductivity in Nanowires: Fabrication and Quantum Transport* (Wiley-VCH, 2012).

[39] Yu. M. Ivanchenko and L. A. Zil'berman, The Josephson effect in small tunnel contacts, Sov. Phys. JETP **28**, 1272 (1969).

[40] See Supplemental Material at http://link.aps.org/supplemental/10.1103/PhysRevApplied.14.034055 for a full description of the theoretical model, the spectral characterization of the active region, the thermal-transport measurements, and the calculation of the sensing performance. It includes Refs. [49–54].

[41] H. J. S. van der Zant, F. C. Fritschy, W. J. Elion, L. J. Geerlings, and J. E. Mooij, Field-Induced Superconductor-To-Insulator Transitions in Josephson-Junction Arrays, Phys. Rev. Lett. **69**, 2971 (1992).

[42] H. Courtois, M. Meschke, J. T. Peltonen, and J. P. Pekola, Origin of Hysteresis in a Proximity Josephson Junction, Phys. Rev. Lett. **101**, 067002 (2008).

[43] J. Bardeen, Critical fields and currents in superconductors, Rev. Mod. Phys. **34**, 667 (1962).

[44] A. F. Andreev, The thermal conductivity of the intermediate state in superconductors, JETP **66**, 1228 (1964).

[45] F. Giazotto, T. T. Heikkilä, A. Luukanen, A. M. Savin, and J. P. Pekola, Opportunities for mesoscopics in thermometry and refrigeration: Physics and applications, Rev. Mod. Phys. **78**, 217-274 (2006).

[46] A. V. Timofeev, C. Pascual Giarcía, N. B. Kopnin, A. M. Savin, M. Meschke, F. Giazotto, and J. P. & Pekola, Recombination-Limited Energy Relaxation in

a Bardeen-Cooper-Schrieffer Superconductor, Phys. Rev. Lett. **102**, 017003 (2009).

[47] P. G. De Gennes, Boundary effects in superconductors, Rev. Mod. Phys. **36**, 225 (1964).

[48] V. G. Kogan, Coherence length of a normal metal in a proximity system, Phys. Rev. B **26**, 88 (1982).

[49] V. Ambegaokar and B. I. Halperin, Voltage due to Thermal Noise in the dc Josephson Effect, Phys. Rev. Lett. **22**, 1364 (1969).

[50] A. F. Andreev, Thermal conductivity of the intermediate state of superconductors. II, Sov. Phys. JETP **20**, 1490 (1965).

[51] F. C. Wellstood, C. Urbina, and J. Clarke, Hot-electron effects in metals, Phys. Rew. B **49**, 5942 (1994).

[52] T. T. Heikkilä, M. Silaev, P. Virtanen, and F. S. Bergeret, Thermal, electric and spin transport in superconductor/ ferromagnetic-insulator structures., Prog. Surf. Sci. **94**, 100540 (2019).

[53] H. Rabani, F. Taddei, O. Bourgeois, R. Fazio, and F. Giazotto, Phase-dependent electronic specific heat in mesoscopic josephson junction, Phys. Rev. B **78**, 012503 (2008).

[54] T. Bergmann, Phd Dissertation, University of Utrecht, 2004.